





Article

Putting Abandoned Farmlands in the Legend of Land Use and Land Cover Maps of the Brazilian Tropical Savanna

Ivo Augusto Lopes Magalhães ¹, Edson Eyji Sano ^{2,*}, Édson Luis Bolfe ³ and Gustavo Bayma ⁴

¹ Institute of Geosciences, University of Brasília, Brasília 70910-900, Brazil

² Brazilian Agricultural Research Corporation (Embrapa Cerrados), Planaltina 73301-970, Brazil

³ Brazilian Agricultural Research Corporation (Embrapa Agricultura Digital), Campinas 13083-886, Brazil; edson.bolfe@embrapa.br

⁴ Brazilian Agricultural Research Corporation (Embrapa Meio Ambiente), Jaguariúna 13820-000, Brazil; gustavo.bayma@embrapa.br

* Correspondence: edson.sano@embrapa.br

Abstract

Farmland abandonment is becoming a growing land use challenge in the Brazilian Cerrado, yet its extent, spatial distribution, and underlying drivers remain poorly understood. This study addresses the following question: Can deep learning methods reliably identify abandoned farmlands in tropical savanna environments using multispectral satellite images? To answer this question, we used a Fully Connected Neural Network (FCNN) classifier to map abandoned farmlands in the municipality of Buritizeiro, Minas Gerais State, Brazil, using Sentinel-2 images acquired in 2018 and 2022. Seven land use and land cover (LULC) classes were mapped using visible and near-infrared bands, spectral indices, spectral mixture components, and principal components as input parameters for the CNN. The LULC map for 2022 achieved high classification performance (overall accuracy = 94.7%; Kappa coefficient = 0.93). Agricultural areas classified in 2018 as annual croplands, cultivated pastures, eucalyptus plantations, or harvested eucalyptus that transitioned to grasslands or shrublands in 2022 were considered abandoned. Based on this definition, we identified 13,147 hectares of abandoned land in 2022, representing 4.7% of the municipality's agricultural area in 2018. Most abandoned areas corresponded to eucalyptus plantations established for charcoal production. This study provides the first deep learning-based assessment of farmland abandonment in the Cerrado. Our findings demonstrated the potential of FCNN classifiers for detecting abandoned farmlands in this biome and provide important contribution for public policies focused on ecological restoration, carbon sequestration, and sustainable agricultural planning.

Keywords: tropical savanna; deep learning; remote sensing; Sentinel-2



Academic Editors: Paul Aplin,
Elias Symeonakis and Moses
Azong Cho

Received: 31 October 2025

Revised: 20 December 2025

Accepted: 25 December 2025

Published: 27 December 2025

Copyright: © 2025 by the authors.

Licensee MDPI, Basel, Switzerland.

This article is an open access article distributed under the terms and

conditions of the [Creative Commons Attribution \(CC BY\)](https://creativecommons.org/licenses/by/4.0/) license.

1. Introduction

Farmland abandonment is becoming an increasingly significant land use transition in numerous countries [1–4]. Despite its growing relevance for agricultural planning, ecological restoration, and regional sustainability, the extent and spatial distribution of abandoned agricultural land remain poorly quantified in several regions of the world. In Brazil, existing national and regional land use datasets do not explicitly identify abandoned farmland, limiting the capacity of policymakers and land managers to monitor this process or assess its environmental and socio-economic implications.

Abandoned farmlands are defined as previously cultivated areas that have ceased active agricultural production and remain unmanaged, uncultivated, or underutilized for more than one year, typically between two and five years, depending on the author [5–7]. More specifically, the most essential concept of abandoned farmland is the interruption or discontinuation of active agricultural use on land that was previously cultivated or managed. This includes stopping crop cultivation (e.g., soybean, maize, and sugarcane), suspending cultivated pasture maintenance such as grazing rotation, fertilization, liming, or weed control, and interrupting harvesting cycles, such as those of eucalyptus plantations. Abandonment is defined based on a minimum period without agricultural use. This threshold varies among authors and regions, typically ranging from at least 1 to 5 or more years [8]. A common understanding in the literature is that abandoned farmland undergoes ecological secondary succession, with vegetation gradually returning to a more original state. This process is characterized by an increase in native grasses, shrubs, and trees, regardless of the type of previous agricultural use. Remote sensing-based studies typically identify abandoned farmland by detecting shifts in spectral signatures from cultivated land to natural vegetation.

This phenomenon is widespread globally, especially in Russia (12.4 million hectares), China (8.7 million hectares), and Brazil (8.4 million hectares) [3,9]. Farmland abandonment has important implications for food security and is driven by a complex combination of social, economic, and environmental factors. Common drivers include logistical constraints in remote regions with limited accessibility and high transportation costs; soil and water degradation that reduces agricultural productivity; land reform processes; rural-to-urban migration; inheritance disputes; aging farming population; unfavorable agricultural input and product prices; and, in some contexts, armed conflicts [2,10–13]. Farmland abandonment can also occur even in areas with favorable agricultural conditions [14]. Despite its challenges, abandonment can generate important environmental benefits, including the natural regeneration of native vegetation, increased carbon sequestration, improved wildlife habitat, and enhanced nutrient cycling [15].

The Brazilian Cerrado has experienced extensive agricultural expansion and remains a major center of intensive land development, mostly driven by large-scale grain production for export, mainly soybean, corn, and cotton [16–18]. The Cerrado is not only a global biodiversity hotspot [19] but also a socio-economic pillar of Brazil, sustaining decades of rapid and sustained agribusiness growth [20]. Covering roughly 200 million hectares, the biome supports the country's agricultural economy by producing more than half of Brazil's grain exports and supporting extensive livestock systems that supply both domestic and international markets [17].

Over the past four decades, technological innovations, soil correction practices, and large-scale mechanization have transformed vast areas of the Cerrado into one of the world's most competitive agricultural frontiers, generating export revenues that are critical to Brazil's gross domestic product (GDP) [21,22]. Despite these advances, the region continues to face persistent socio-economic and environmental challenges, including land concentration, increasing production costs, high water demand for irrigation, and soil and water pollution resulting from excessive use of fertilizers [23,24].

The municipality of Buritizeiro, located in northern Minas Gerais State in a transitional zone toward the semi-arid Caatinga biome, ranks among the top ten hotspots of farmland abandonment in the Cerrado [25]. One of the main limiting factors in the region is low annual precipitation, which reduces pasture biomass production and compromises livestock feeding, especially during the six-month dry season (April to September) [26,27]. During this period, ranchers rely heavily on purchased forage and mineral supplements,

substantially increasing production costs. This dependence often turns livestock operations economically unviable, leading many landowners to abandon their pastures.

A similar pattern is observed in eucalyptus plantations, which in Buritizeiro are primarily cultivated for charcoal production to supply steel mills in Sete Lagoas, Minas Gerais, approximately 300 km away. The expansion of eucalyptus plantations in the region began in the 1960s, driven mainly by Federal Law No. 5.106/1966, which provided tax incentives for forestry projects, as well as by the widespread availability of low-priced lands [28]. More recently, increasing transportation costs have undermined the profitability of charcoal production, contributing to the widespread abandonment of eucalyptus plantations.

Given the vast extent of the Cerrado biome, mapping and monitoring land use and land cover (LULC) dynamics rely heavily on satellite imagery. These datasets are commonly processed on cloud computing platforms using data-driven classifiers that employ machine learning and deep learning techniques (e.g., [29,30]). Among supervised machine learning algorithms, Random Forest (RF) and Support Vector Machine (SVM) are the most widely applied, while Convolutional Neural Networks (CNNs) have gained increasing prominence within deep learning approaches. RF and SVM often produce high accuracies in LULC classification tasks [31], whereas CNNs are especially effective for detecting LULC changes in complex and heterogeneous landscapes [32]. However, CNN architectures typically involve a large number of layers, which greatly increases the number of parameters, computational requirements, training time, and overall processing costs.

Farmland abandonment represents a distinct land use process in the Cerrado, differing fundamentally from both active agricultural production and conserved natural vegetation. Abandoned areas follow unique trajectories of vegetation regrowth, carbon accumulation, soil recovery, and biodiversity return, and thus cannot be adequately represented by broad LULC classes such as “grassland” or “shrubland.” Treating abandonment as a separate category in the LULC maps allows us to distinguish fragments of natural vegetation from secondary vegetation arising after land use cessation, which differ in ecological functions and restoration potential. Without explicitly mapping abandoned areas, policymakers and land managers lack the necessary information to quantify the extent of underutilized land or to understand the socioeconomic drivers behind these transitions. Therefore, the inclusion of abandoned farmland as a distinct LULC class is scientifically and operationally justified, providing critical insights that cannot be derived from traditional vegetation classes alone.

To the best of our knowledge, no initiatives have specifically focused on mapping abandoned farmlands in the Brazilian Cerrado using deep learning approaches. Only a few studies in the biome have relied on time series of LULC data to map abandoned farmlands. In these studies, pixels corresponding to agricultural lands that transition into natural vegetation over a defined period are classified as abandoned. This is exemplified by the study of Santos and Ruchkys [33], who identified nearly four million hectares of abandoned farmland in the Matopiba region between 2006 and 2018. Matopiba represents the Brazil’s newest agricultural frontier, located in the northernmost portion of the Cerrado biome. Their assessment was based on the country’s annual LULC dataset derived from historical Landsat images processed on the Google Earth Engine platform.

CNNs and fully connected neural networks (FCNNs) are among the most widely used architectures in deep learning [34,35]. In an FCNN, every neuron in a given layer is connected to all neurons in the subsequent layer. Both FCNNs and CNNs typically comprise an input layer, one or more hidden layers, and an output layer, and are commonly used for pixel-based classification tasks. Judith et al. [36], for example, used four vegetation indices derived from multiple agricultural sites as input features for an FCNN to classify crop health with high precision. In their study, the FCNN outperformed SVM, RF, K-

Nearest Neighbors (KNN), and Decision Tree classifiers. Other studies have applied FCNN architectures in domains less directly related to LULC mapping, such as bathymetry estimation [37] and pest occurrence prediction in agricultural lands [38].

The objective of this study was to apply an FCNN-based deep learning approach to Sentinel-2 multispectral images from 2018 to 2022 to identify abandoned farmlands in the municipality of Buritizeiro. Although farmland abandonment mapping has been widely conducted in Europe and Asia [39–41], this study represents the first effort to identify and quantify this phenomenon in the Cerrado biome using deep learning method.

2. Materials and Methods

2.1. Study Area

The study area corresponds to the municipality of Buritizeiro, located in the northern portion of Minas Gerais State, Brazil. The municipality covers 7249 km² and extends between 16°30'–18°00' S latitude and 44°47'–45°33' W longitude (Figure 1). According to the Köppen climate classification, the region has a tropical savanna climate (Aw), characterized by dry, cool winters and hot, rainy summers [42]. The average elevation is 648 m. Mean annual rainfall ranges from 1000 to 1300 mm, while mean monthly temperatures vary from 18 °C in the coldest month to 24 °C in the warmest months.

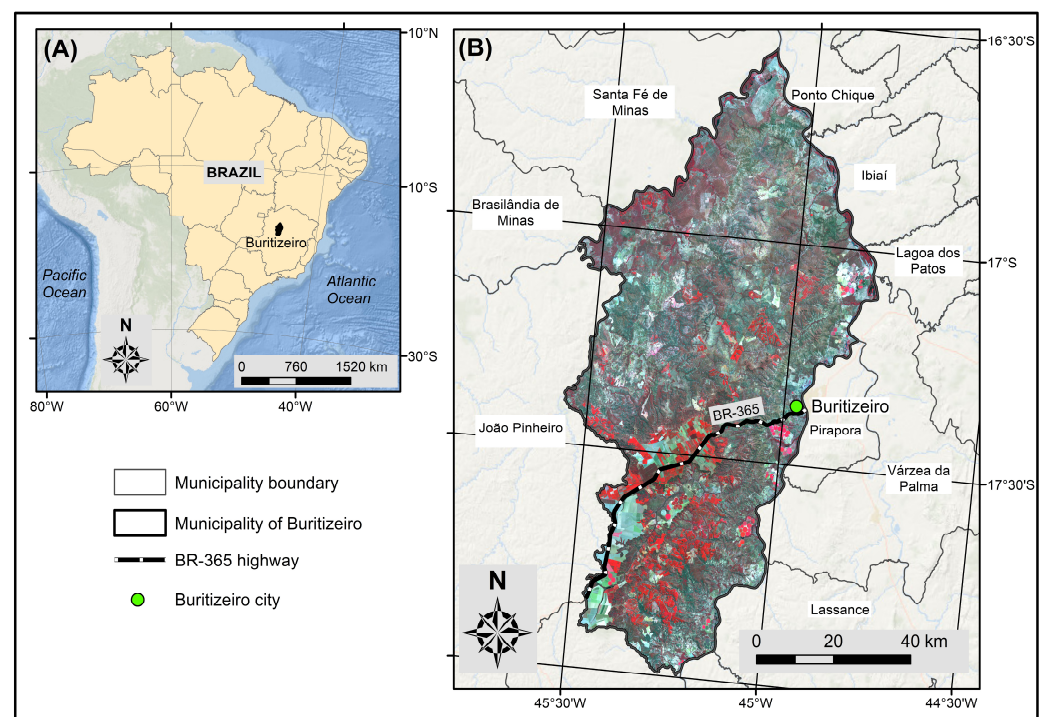


Figure 1. Location of the study area in Brazil (A) and in Minas Gerais State (B). The background image is an RGB false-color composite of bands 8, 4 and 3, generated from Sentinel-2 imagery acquired in 2022.

Buritizeiro is located within the Cerrado biome, which covers approximately 200 million hectares in central Brazil. Currently, about 46% of the biome is occupied by anthropogenic land uses, predominantly cultivated pastures and croplands. Croplands include annual crops (e.g., soybean, maize), semi-perennial crops (e.g., sugarcane), and perennial crops (e.g., coffee). Cultivated pastures, especially those dominated by *Urochloa* and *Andropogon* species, are widespread throughout the biome, while rainfed croplands are mainly concentrated on extensive plateaus that support highly mechanized agricultural systems [20].

Previous studies aiming to discriminate LULC classes have predominantly relied on reflectance information from the red, near-infrared (NIR), and shortwave infrared (SWIR) regions of the electromagnetic spectrum, which are especially sensitive to vegetation structure, moisture content, and soil background. These bands are often transformed into spectral indices such as the Normalized Difference Vegetation Index (NDVI) [43,44], Enhanced Vegetation Index (EVI) [45], Bare Soil Index (BSI) [46,47], and Normalized Difference Water Index (NDWI) [48], which help enhance subtle spectral contrasts and reduce radiometric variability. Such indices have been extensively used to highlight differences in canopy vigor, soil exposure, and surface moisture, improving the separability of vegetation types, agricultural crops, and degraded or abandoned areas.

2.2. Methods

Figure 2 presents the main methodological framework adopted in this study. The approach involved the acquisition of two cloud-free (<5% cloud cover) Sentinel-2 Multi-spectral Imager (MSI) Level-2A and Level-2B surface reflectance scenes from 15 August 2018 and 19 August 2022, respectively [49]. Sentinel-2 Level-2A is the standard product distributed by the European Space Agency (ESA), providing surface reflectance data corrected for atmospheric effects, whereas Level-2B products correspond to Level-2A data further corrected for Bidirectional Reflectance Distribution Function (BRDF) effects [50]. All images were obtained from the Google Earth Engine platform. For each acquisition date, bands 2 (blue), 3 (green), 4 (red), and 8 (near-infrared), each with a spatial resolution of 10 m, were selected for analysis (Table 1). All datasets were projected to the Universal Transverse Mercator (UTM) projection system, zone 23S, covering a swath width of 290 km.

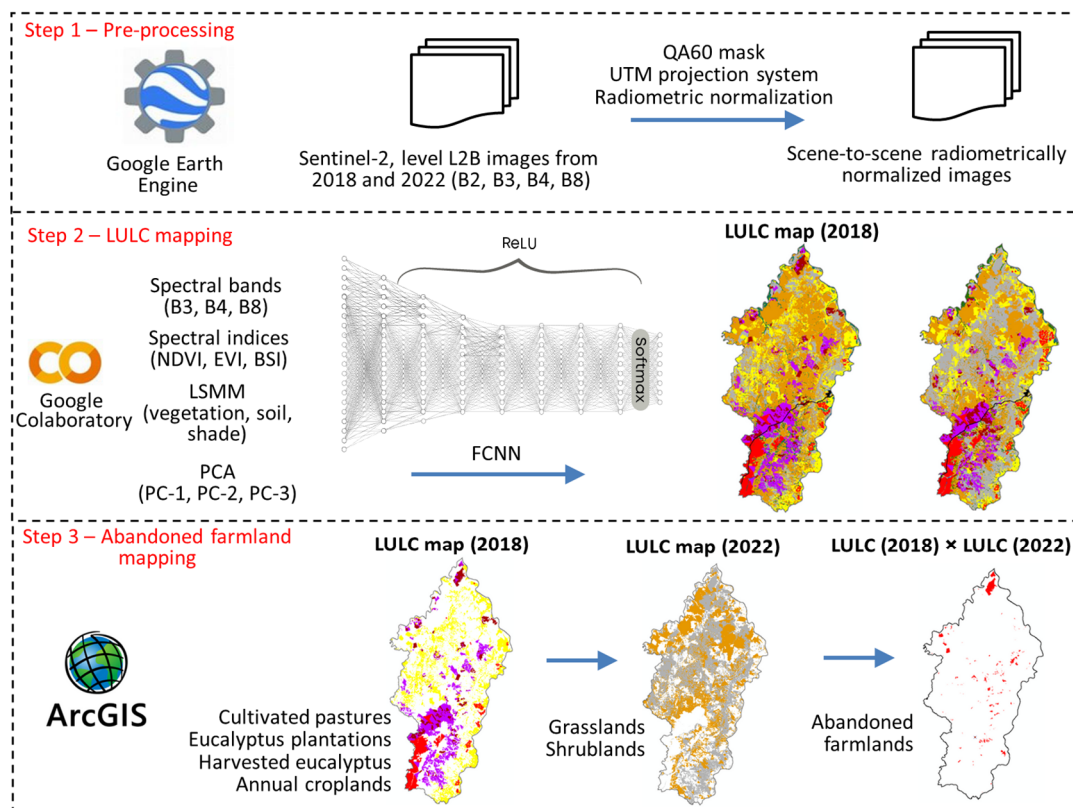


Figure 2. Flowchart of the main methodological steps. UTM = Universal Transverse of Mercator; NDVI = Normalized Difference Vegetation Index; EVI = Enhanced Vegetation Index; BSI = Bare Soil Index; LSMM = Linear Spectral Mixture Model; PCA = Principal Component Analysis; PC = principal components; ReLU = rectified linear unit; FCNN = fully connected neural network; and LULC = land use and land cover.

Table 1. Characteristics of the Sentinel-2 satellite images acquired in this study. MSI = Multispectral Imager; NIR = near-infrared.

Satellite	Acquisition Date	Processing Level	Spatial Resolution (m)	Spectral Bands	Cloud Cover (%)
Sentinel-2 MSI	15 August 2018	L2A	10	B2 (Blue), B3 (Green), B4 (Red), B8 (NIR)	0.58
Sentinel-2 MSI	19 August 2022	L2B	10	B2 (Blue), B3 (Green), B4 (Red), B8 (NIR)	0.68

Source: ESA [50].

2.2.1. Pre-Processing

The cloud-contaminated pixels in the Sentinel-2 images used in this study were removed using the QA60 mask band. This band is a quality-assurance bitmask that provides per-pixel information on cloud and cirrus contamination: uncontaminated pixels have a value of 0, whereas pixels affected by clouds and cirrus are assigned values of 1024 and 2048, respectively. In addition, radiometric normalization based on z-score standardization was applied to minimize interannual variability in illumination and atmospheric conditions, ensuring comparability between the two acquisition dates.

The images were reprojected to the UTM projection system, Zone 23S, using the SIRGAS2000 datum. Bands B2, B3, B4, and B8 were then composited into a single multi-band file and clipped to the administrative boundary of the municipality of Buritizeiro, obtained from the Brazilian Institute of Geography and Statistics (IBGE) in vector format at a 1:250,000 scale [51]. All pre-processing steps were performed on the Google Earth Engine platform.

2.2.2. LULC Mapping

The following spectral indices were derived from the Sentinel-2 images and employed as input parameters for the supervised deep learning classification (Table 2): NDVI, EVI, and BSI. NDVI is the most widely applied vegetation index because of its high sensitivity to variations in photosynthetic activity. EVI is more responsive to canopy structure and less affected by soil background and atmospheric interference. BSI is especially effective for distinguishing agricultural from non-agricultural areas by enhancing the spectral response of bare and fallow soils. Additionally, Sentinel-2 bands 3, 4, and 8 were processed using the Linear Spectral Mixture Model (LSMM) [52] to generate vegetation, soil, and shade fraction images. This model assumes that the reflectance of each pixel is a linear combination of the spectral contributions from key land cover components and can be expressed as follows [53] (Equation (1)):

$$R_i = \sum_{j=1}^n f_j r_{i,j} + \varepsilon_i \quad (1)$$

where R_i represents the spectral reflectance in the i th spectral band; $r_{i,j}$ is the spectral reflectance of the j th component in spectral band i th (endmember); f_j is the proportion of the j th component within the pixel; and ε_i is the residual for the spectral band i th.

Table 2. Spectral vegetation indices used in this study for the deep learning classification procedure. NDVI = Normalized Difference Vegetation Index; EVI = Enhanced Vegetation Index; BSI = Bare Soil Index; ρ = surface reflectance; BLUE = blue band; RED = red band; and NIR = near-infrared band.

Vegetation Index	Abbreviation	Formula	Citation
Normalized Difference Vegetation Index	NDVI	$NDVI = \frac{\rho_{NIR} - \rho_{RED}}{\rho_{NIR} + \rho_{RED}}$	Rouse et al. [43]
Enhanced Vegetation Index	EVI	$EVI = 2.5 + \frac{\rho_{NIR} - \rho_{RED}}{\rho_{NIR} + 6 \times \rho_{RED} - 7.5 \times \rho_{BLUE} + 1}$	Huete et al. [45]
Bare Soil Index	BSI	$BSI = 1 + \frac{(\rho_{SWIR} + \rho_{RED}) - (\rho_{NIR} + \rho_{BLUE})}{(\rho_{SWIR} + \rho_{RED}) + (\rho_{NIR} + \rho_{BLUE})}$	Polykretis et al. [47]

Finally, the three spectral bands were processed using Principal Component Analysis (PCA), a widely applied multivariate statistical technique over several scientific disciplines [54]. The resulting principal components were then combined with the vegetation indices and LSM fraction images to train the FCNN model [55].

The FCNN architecture consisted of nine hidden layers with 2048, 1024, 512, 256, 128, 64, 16, 8, and 8 neurons, respectively. The Rectified Linear Unit (ReLU) activation function was applied to all hidden layers, and the Softmax function was used in the output layer. Model training was conducted with the Adam optimizer to minimize the categorical cross-entropy loss function. The model was trained for 500 epochs with a batch size of 16, using a 60/40 split between the training and validation datasets.

The methodological workflow was implemented in Python 3.14.0 using the scikit package, which integrates machine learning and deep learning frameworks such as scikit-learn and TensorFlow. These frameworks provide robust tools for modeling and are well-suited for handling the complexity of remote sensing data. All implementations were executed on a virtual instance within the Google Colaboratory environment.

For the FCNN classification, eight LULC classes were considered: forestlands, shrublands, grasslands, cultivated pastures, annual croplands, eucalyptus plantations, harvested eucalyptus, and water bodies. Urban area and center-pivot irrigated fields were manually delineated and excluded from the classification.

The training, validation, and testing datasets were derived from 154 field sampling points collected in June and August 2023. At each site, the dominant LULC class was recorded along with Global Positioning System (GPS) coordinates, and panoramic photographs were taken using a conventional digital camera with 7.1-megapixel resolution. These field data were complemented by visual interpretation of high-resolution Google Earth images, resulting in a total of 2240 samples for training (70%), 640 for validation (20%), and 320 for testing (10%) (Figure 3). Each sample corresponded to a circular area with a 20 m radius. The accuracy of the FCNN classification was assessed based on the confusion matrix, Kappa coefficient, overall accuracy, and omission and commission errors.

The rates of change among LULC classes during the 2018–2022 period were analyzed using an area-based transition table. Transition tables provide a simple mathematical method for analyzing LULC dynamics between two time periods or between study areas of different sizes [56]. The approach proposed Takada et al. [55] provides an important methodological foundation for converting land use transition matrices derived from multiple and irregular time intervals into comparable annual transition probability models. As highlighted by those authors, satellite observations are often unavailable at consistent dates, and therefore transition matrices from different periods cannot be directly compared without appropriate normalization. These authors address this issue by proposing the computation of the c -th root of a transition matrix to derive annualized transition probabilities.

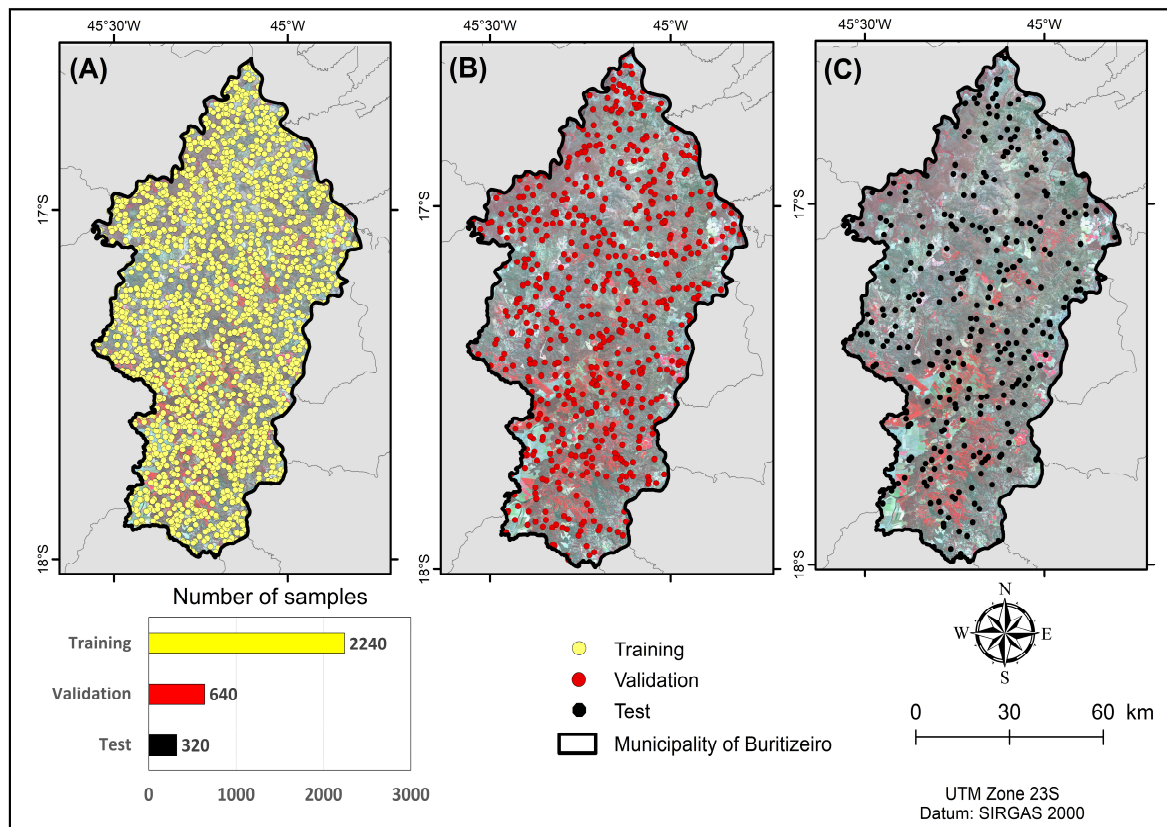


Figure 3. Sampling sites for the Fully Connected Neural Network (FCNN) algorithm: (A) training dataset; (B) validation dataset; and (C) testing dataset.

However, the full application of this approach is not feasible for our dataset because the present study relies on only two LULC maps (2018 and 2022). A two-date transition matrix identifies only the initial and final land use states and does not uniquely determine intermediate trajectories, which prevents the estimation of annual transition probabilities or the comparison of transition rates across periods. For this reason, we retained an area-based transition table as the most appropriate representation of LULC dynamics in our study. A transition table is represented as a square matrix in which rows correspond to classes in the initial year (e.g., 2018) and columns correspond to classes in the final year (e.g., 2022). Each cell indicates the amount of area (e.g., hectares) that transition from class i to class j during the study period.

The rate of suppression of native vegetation in the study area was estimated considering the formula proposed by [57] (Equation (2)):

$$r = \frac{1}{t_2 - t_1} \ln \left(\frac{A_2}{A_1} \right) \quad (2)$$

where A_1 is the area of native vegetation at initial date; A_2 is the area of native vegetation at final date; and $t_2 - t_1$ is the number of years.

The main advantage of the Puyravaud [57] formula is that it is scale-invariant and logarithmic, allowing it to represent realistic rates of change even when time intervals differ; when the magnitude of change is very large or very small; when initial and final areas differ substantially; or when deforestation and regrowth follow nonlinear trajectories. For these reasons, the Puyravaud approach is more advantageous than, for example, the linear proportion-based method proposed by Lemessa [58], which may underestimate or overestimate rates under conditions of strong change, or the method introduced by

Xinchang et al. [59], which does not standardize rates across time intervals and therefore produces values that vary according to the length of the monitoring period.

2.2.3. Farmland Abandonment Mapping

Agricultural areas mapped in 2018 as annual croplands, cultivated pastures, eucalyptus plantations, or harvested eucalyptus that were reclassified as grasslands or shrublands in 2022 were identified as abandoned farmlands. The resulting raster-based change map was post-processed using the *sieve* tool in QGIS to remove isolated patches smaller than 100 pixels and was subsequently converted to vector format for further spatial analysis.

The accuracy of the final farmland abandonment map was assessed through systematic visual interpretation of high-resolution satellite images available on the Google Earth platform. To reduce potential uncertainty associated with edge effects in medium-resolution images, only polygons larger than 10 hectares were included in this evaluation. Accuracy assessment was based on overall accuracy and the Kappa coefficient [60,61]. Overall accuracy (OA) corresponds to the ratio between number of correctly classified samples and the total number of samples (Equation (3)).

$$OA = \frac{\sum_{i=1}^k n_{ii}}{N} \quad (3)$$

where n_{ii} is the correctly classified samples for class i ; k is the number of classes; and N is the total number of reference samples.

The Kappa coefficient measures the level of agreement between the classified map and the reference data, corrected for the agreement that could occur randomly (Equation (4)).

$$k = \frac{P_o - P_e}{1 - P_e} \quad (4)$$

where P_o is the observed proportion of agreement (equivalent to overall accuracy), and P_e is the expected proportion of agreement due to chance. For a larger number of classes, the Kappa coefficient typically ranges between 0 and 1.

2.2.4. Processing Tools

Several software platforms and processing environments were used throughout this study. Google Earth Engine was employed for image acquisition and all pre-processing steps, including cloud masking, radiometric normalization, reprojection, and image clipping. It was also used to generate spectral composites and extract the spectral variables required as input parameters for the subsequent classification procedures. The Sentinel Application Platform (SNAP) version 11.0.0 was used to generate Sentinel-2 mosaics and to examine sensor-specific radiometric properties.

The TerraAmazon 7.3.3 platform, developed by the National Institute for Space Research (INPE), was used to compute the NDVI, EVI, and BSI spectral indices. ArcGIS 10.2 was employed for spatial analysis tasks, post-classification vectorization, and cartographic production. QGIS Desktop 3.34 was used to refine post-classification outputs, especially for removing isolated patches smaller than 100 pixels and converting raster outputs to vector format. The deep learning models were implemented in Python through the scikiteo package, which integrates scikit-learn and TensorFlow libraries. Model training, validation, and testing were conducted in the Google Colaboratory environment, which provided the computational resources necessary for running the FCNN architecture and managing the large number of model parameters.

3. Results

Figure 4 presents examples of field photographs representing the main LULC classes identified in the study area. These include natural vegetation (forestlands, shrublands, and grasslands), agricultural land uses (cultivated pastures, annual croplands, eucalyptus plantations, and harvested eucalyptus), and two categories of abandoned agricultural land: abandoned eucalyptus plantations and abandoned cultivated pasturelands.

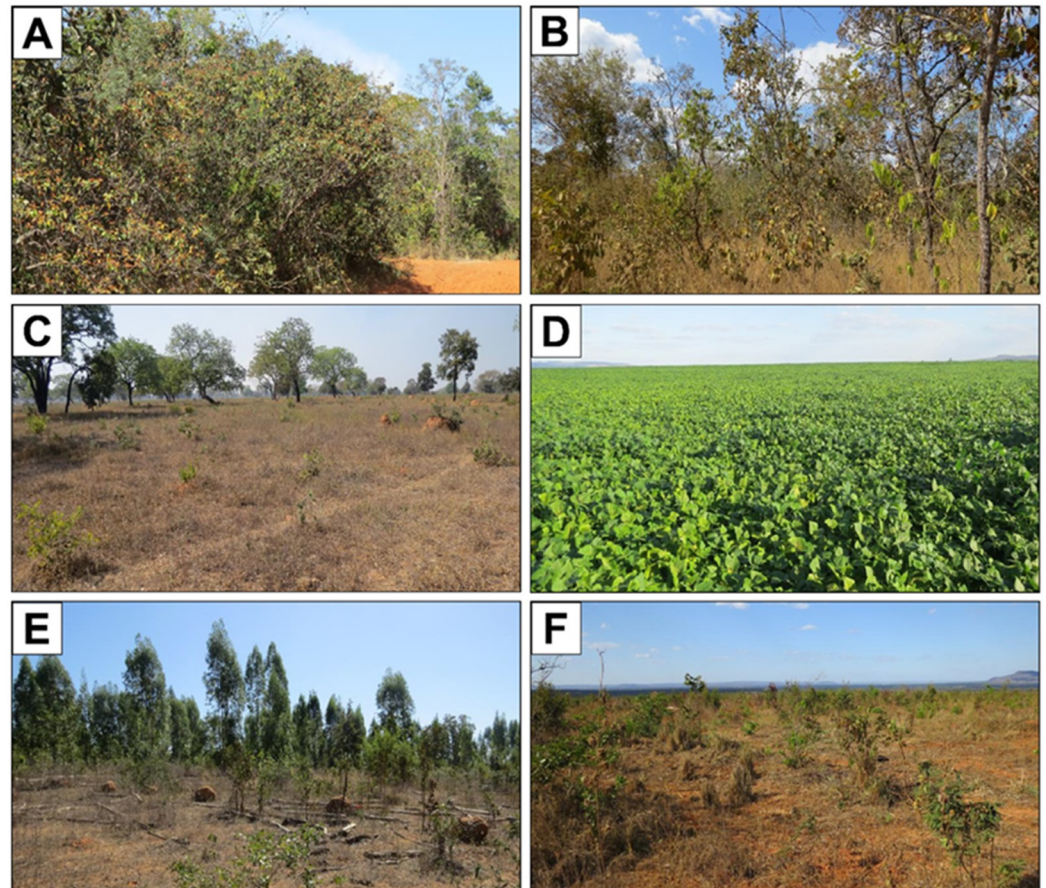


Figure 4. Field photographs illustrating examples of the main land use and land cover classes identified in the municipality of Buritizeiro, Minas Gerais State, Brazil. Photographs were taken between 20 and 23 June 2023. (A) forestland; (B) shrubland; (C) cultivated pasture with *Brachiaria* species; (D) soybean field; (E) abandoned eucalyptus plantation; and (F) abandoned cultivated pasture.

3.1. Land Use and Land Cover Mapping

The LULC classes mapped for 2018 and 2022 in the municipality of Buritizeiro are presented in Figures 5 and 6, respectively. Prior to analysis, the classification results were smoothed using a 100-pixel threshold filter to reduce isolated noise. In this case, the sieve function available in QGIS was applied. This tool removes small, isolated pixel groups from a classified raster by replacing them with the value of the largest adjacent neighboring class.

Among the native vegetation formations, shrublands represented the largest class, covering 37% of the municipality in 2018 and 26% in 2022, and were widely distributed throughout the area. Grasslands were also widespread, occupying 18% of the municipality in 2018 and 27% in 2022. Forestlands accounted for approximately 5% of the area and were mainly concentrated along river courses, forming characteristic gallery forests [62].

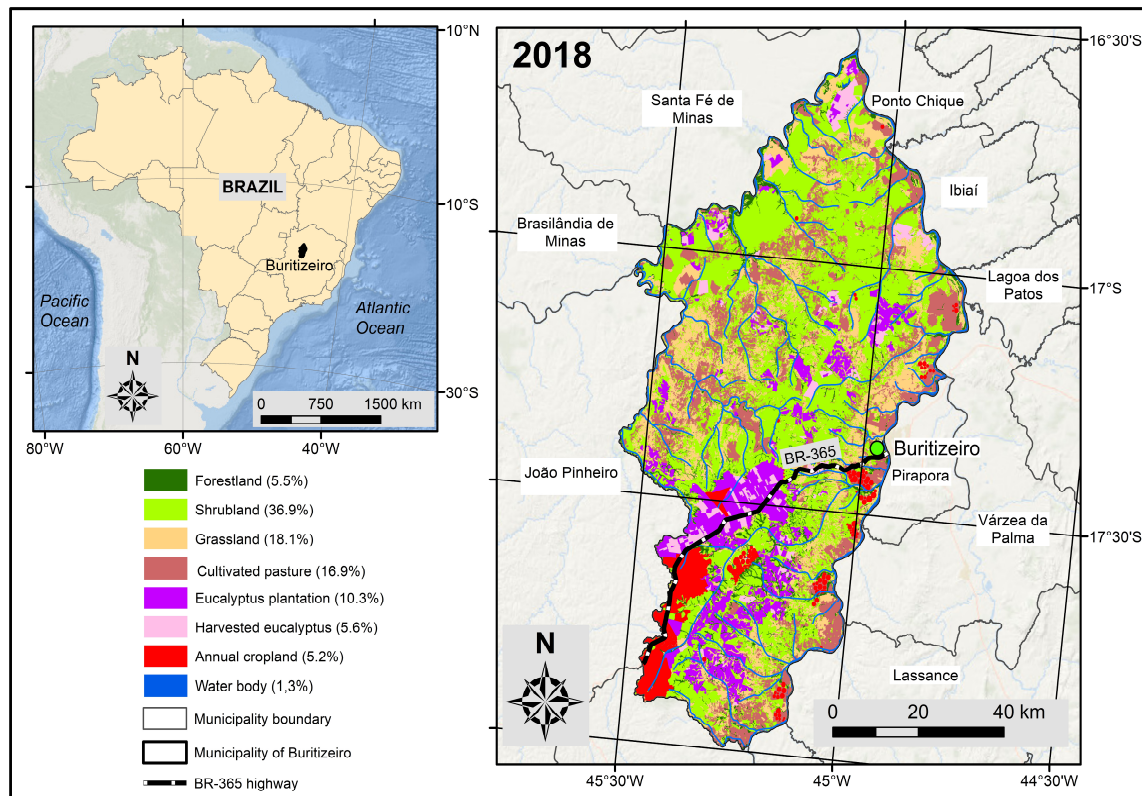


Figure 5. Land use and land cover map of the municipality of Buritizeiro, Minas Gerais State, from 2018.

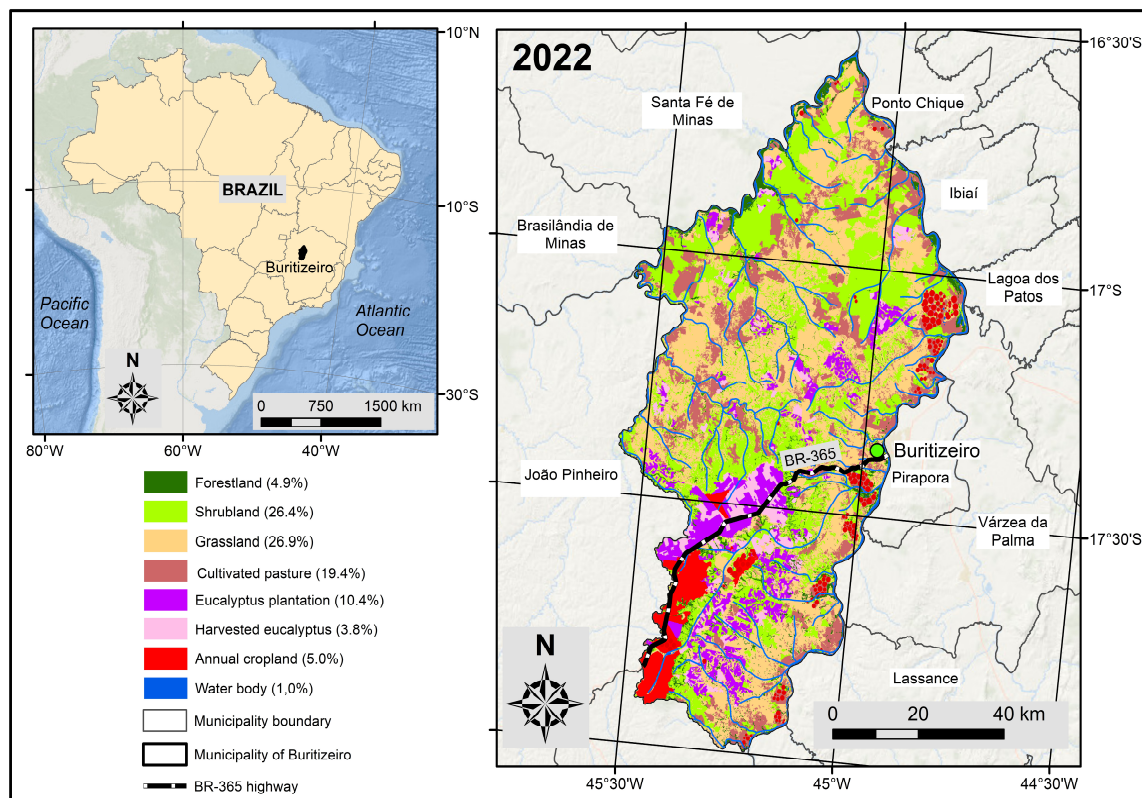


Figure 6. Land use and land cover map of the municipality of Buritizeiro, Minas Gerais State, from 2022.

Table 3 presents the 2018–2022 transition table for the main LULC classes in the municipality of Buritizeiro. This table summarizes how each class mapped in 2018 either changed or remained stable by 2022, allowing the quantification of gains, losses, and major transitions among classes. These patterns highlight the dominant processes of vegetation dynamics and agricultural expansion or intensification occurring in the region during the study period. Water bodies and urban areas were not included in the table, as their extent was assumed to remain essentially unchanged over the five-year interval. A notable result shown in the transition table is the loss of 12,433 hectares of eucalyptus plantations and harvested eucalyptus from 2018 to 2022.

Table 3. Area-based (hectares) transition table among land use categories in the municipality of Buritizeiro, Minas Gerais State, Brazil.

2018	2022	2022	2022	2022	2022	2022	2022	2018
	Forestland	Shrubland	Grassland	Cultivated Pasture	Eucalyptus Plantation	Harvested Eucalyptus	Annual Crops	Total
Forestland	16,349	9980	5177	1010	437	226	78	33,257
Shrubland	7536	160,725	99,103	23,324	3027	4028	502	298,245
Grassland	2819	16,550	87,083	15,800	641	800	277	123,970
Cultivated pasture	1266	6896	51,571	59,892	575	959	18	121,177
Eucalyptus plantation	692	3322	6519	1743	43,709	17,541	895	74,421
Harvested eucalyptus	101	1263	6289	2817	8446	5493	18	24,427
Annual crops	53	313	503	83	465	68	21,146	22,631
Total	28,816	199,049	256,245	104,669	57,300	29,115	22,934	698,128

Considering that native vegetation formations (forestlands, shrublands, and grasslands) occupied 60.5% of the total area of Buritizeiro in 2018 and 58.2% in 2022 (Figures 5 and 6), native vegetation declined at an average rate of 0.95% per year during the five-year period, according to the formulation proposed by Puyravaud [57]. This rate is substantially higher than the suppression rate estimated using MapBiomass LULC data for the same years, which corresponded to 0.15% per year [63]. The higher rate of native vegetation loss derived from Sentinel-2 images is likely explained by a combination of factors, including differences in spatial resolution (10 m vs. 30 m), classification methodology (deep learning vs. machine learning) and temporal compositing (single overpass vs. annual mosaics).

3.2. Abandoned Farmlands

The spatial distribution of abandoned agricultural areas in Buritizeiro between 2018 and 2022 was derived from a temporal analysis of LULC classifications generated by the FCNN method. A total of 13,147 hectares of abandoned farmland was identified within the municipality (Figure 7). Most of these areas (87%) corresponded to eucalyptus plantations or harvested eucalyptus in 2018, representing 4.7% of the municipality's total agricultural land cover. This abandonment rate is nearly four times higher than the 1.2% reported in 2017 for the 31.5 million ha of agricultural land in the Matopiba region, a major agricultural frontier situated in the northern Cerrado [33].

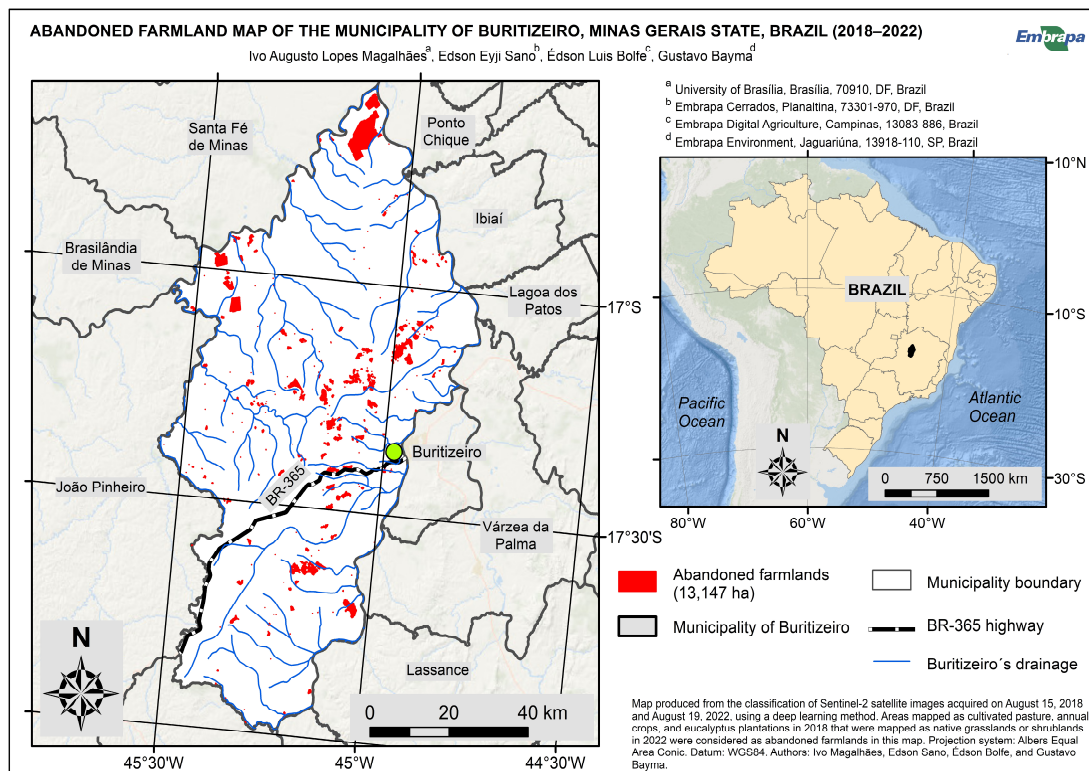


Figure 7. Map of abandoned farmlands in the municipality of Buritizeiro, Minas Gerais State, Brazil, between 2018 and 2022.

4. Discussion

4.1. LULC Mapping Results

In 2018, the municipality of Buritizeiro presented 60% of its territory covered by native vegetation formations, decreasing slightly to 58% in 2020. These results are consistent with MapBiomas data for 2025 [63], which reported that native vegetation covered 52% of the municipality in 2024. The MapBiomas Project is a multi-institutional initiative that annually maps Brazil's LULC classes using 30 m resolution Landsat data processed on the Google Earth Engine platform [64]. As emphasized in previous studies (e.g., [62,65,66], the natural vegetation of the Cerrado forms a mosaic of grasses, shrubs, and trees in varying proportions depending on regional conditions, with gradual transitions among the three dominant formations (grasslands, shrublands, and forestlands). This structural complexity makes accurate classification of Cerrado formations especially challenging, regardless of the imaging sensor or classification algorithm employed.

This study identified approximately 75,000 hectares of eucalyptus plantations in both 2018 and 2022, a result that closely matches with the MapBiomas Project estimate of about 73,000 hectares. These plantations, along with their corresponding harvested areas, were mainly concentrated in the northern and southwestern portions of the municipality, forming relatively large and continuous blocks. Additional occurrences were observed in the western region, especially along the BR-365 highway. No significant expansion of eucalyptus reforestation was detected, as the spatial extent of plantations mapped in 2018 remained largely unchanged in 2022.

A similar spatial distribution and areal extent were observed for annual croplands. Both this study and the MapBiomas Project estimated their coverage at approximately 35,000 hectares, with a strong concentration in the southern portion of the municipality. A high density of center-pivot irrigation systems was recorded along the southeastern boundary, supplied by water resources from the São Francisco River. The extent of irrigated

croplands expanded significantly, from 858 hectares in 2018 to 14,851 hectares in 2022. In contrast, only one abandoned center-pivot system, covering 88 hectares, was identified during the study period. In the Cerrado biome, the abandonment or conversion of center-pivot systems to rainfed agriculture is relatively common. For example, Sano et al. [67] reported that 10% of center-pivots active in 2005 had been deactivated by 2020.

The transition table of the seven main LULC classes in the study area (Table 3) shows that shrubland and grassland showed very high internal persistence, with 160,725 hectares remaining as shrubland and 87,083 hectares remaining as grassland between 2018 and 2022. These two classes constitute the largest land cover types in the region. In contrast, forestland was considerably less stable: only 16,349 hectares persisted as forest, while 16,908 hectares transitioned to other LULC classes, mainly shrubland. Harvested eucalyptus also demonstrated low persistence (5493 ha), reflecting the highly dynamic rotational cycles typical of plantation forestry.

Among natural land cover classes, grasslands showed a strong positive net change (approximately +132,000 ha), indicating substantial conversion from other classes, whereas shrublands showed a strong negative net change (approximately −99,000 ha), reflecting a marked retraction of shrubland vegetation (Figure 8). As discussed earlier, a considerable portion of these opposing trends may be associated with the well-known difficulty of accurately discriminating grassland and shrubland classes using optical remote-sensing data. Among land use classes, both cultivated pastures and eucalyptus plantations exhibited net losses of approximately 17,000 ha each, supporting the interpretation of land use retraction and potential abandonment during the analyzed period.

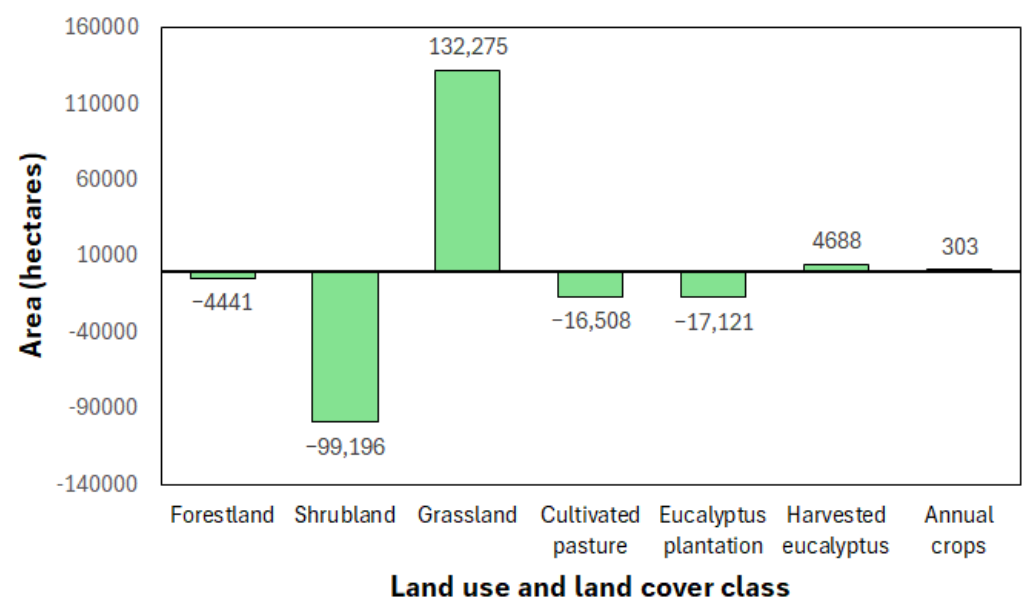


Figure 8. Net land use and land cover changes in the municipality of Buritizeiro between 2018 and 2022.

A notable pattern is the conversion of shrubland to grassland (99,103 hectares) and from shrubland to cultivated pasture (23,324 hectares). These transitions suggest a degradation gradient in which shrublands shift toward more open physiognomies, consistent with grazing pressure and fire regimes commonly observed in the Cerrado (e.g., Arruda et al. [68]). The conversion of grasslands to cultivated pasture (15,800 hectares), as well as the transition from grasslands to shrublands (16,550 hectares) indicates two concurrent processes: agricultural intensification, in which grasslands are converted into productive pastures, and ecological regrowth, in which grasslands transition into shrub-dominated physiognomies. However, as highlighted by Sano et al. [20], distinguishing cultivated

pastures, grasslands, and shrublands using single-date satellite images remains challenging due to their strong spectral similarity, the effects of variable solar illumination conditions during image acquisition, and the pronounced climatic seasonality characteristic of the Cerrado biome.

4.2. LULC Mapping Accuracy

The LULC classification for 2022 achieved an overall accuracy of 94.7% and a Kappa coefficient of 0.933, which is considered excellent according to the Landis and Koch [69] scale (ranging from poor <0.40 to excellent >0.75) and very good on Altman's agreement scale (ranging from poor <0.20 to very good 0.81–1.00) [70] (Table 4). These results are consistent with previous studies, which commonly report accuracies above 85% for relatively similar LULC mapping applications. For example, Basheer et al. [71] obtained overall accuracies ranging from 87% to 94% when comparing three machine learning classifiers applied to Landsat, Sentinel-2, and PlanetScope images over a study area in southern Canada. Likewise, Zhao et al. [72] reported Kappa coefficients of 0.94–0.97 and overall accuracies between 96% and 99% in a LULC classification study conducted in Pakistan using Sentinel-2 images from 2022 and three different machine learning classifiers.

Table 4. Confusion matrix for the Fully Connected Neural Network (FCNN) classification based on Sentinel-2 satellite images, used to discriminate representative land use and land cover (LULC) classes in the municipality of Buritizeiro, Minas Gerais State, Brazil, with a 95% of confidence interval. FOR = forestland; SHR = shrubland; GRA = grassland; PAS = cultivated pasture; EUC = eucalyptus plantation; HAR = harvested eucalyptus; CRO = annual cropland; OE = omission error; and CE = commission error.

	FOR	SHR	GRA	PAS	EUC	HAR	CRO	OE (%)	CE (%)
FOR	12	0	0	0	1	0	0	7.69	14.28
SHR	0	80	4	0	0	0	0	4.76	9.09
GRA	0	8	97	0	0	0	0	7.62	3.96
PAS	0	0	0	48	0	0	0	0	4
EUC	2	0	0	0	24	0	0	7.69	4
HAR	0	0	0	2	0	11	0	15.38	0
CRO	0	0	0	0	0	0	11	0	0

Kappa coefficient: 0.9326 Overall accuracy: 94.69%.

The highest omission error in this study was associated with harvested eucalyptus (15.4%), which was mainly misclassified as eucalyptus plantation. The highest commission error occurred for forestland (14.3%), resulting from the misclassification of non-forest polygons, mainly eucalyptus plantations, as forest due to their structural similarity. Mutual misclassification was also observed between native grasslands and shrublands, reflecting their well-documented spectral resemblance [65,66], with errors ranging from 4% to 9%. In contrast, annual croplands were classified with no omission and commission errors.

4.3. Abandoned Farmlands

The 139 polygons larger than 10 hectares that were classified as abandoned farmlands were visually inspected using a time series of high-resolution satellite images available on the Google Earth platform. This analysis confirmed clear evidence of abandonment in 106 polygons, resulting in an overall accuracy of 76.3%. The remaining polygons corresponded to cultivated pastures, native vegetation (mainly grasslands or shrublands), active Eucalyptus plantations or fallow in some period of the whole period.

We opted not to perform FCNN-based annual classifications for every year of the study period to avoid misidentifying agricultural areas that were intentionally left uncultivated

for short intervals, typically one year, known as fallow. Such temporary resting periods are not considered abandonment in most studies. Additionally, strong climatic seasonality in the region and the high spectral similarity among certain LULC classes (e.g., cultivated pastures vs. natural grasslands) could increase misclassification errors in annual maps. Instead, we relied on visual interpretation of multi-year, high-resolution imagery available on the Google Earth platform. All polygons larger than 10 ha were visually inspected across the entire period, and areas identified as fallow were subsequently treated as omission errors in the accuracy assessment.

Among the 83 abandoned eucalyptus polygons larger than 10 hectares identified in the municipality, totaling 10,487 hectares, the vast majority (78) were located on *Latosolos* (Ferralsols under the FAO classification), while four occurred on *Cambissolos* (Cambisols) and one on *Gleissolos* (Gleysols). In Brazil, eucalyptus plantations are heavily concentrated in Minas Gerais State, which accounts for 24% of the national total. These plantations are typically established on low fertility soils and are primarily used for cellulose, paper, and charcoal production [17,73,74]. In the Buritizeiro region, *Eucalyptus urophylla* is the predominant planted species. As previously mentioned, the primary end use of local eucalyptus production is charcoal manufacturing to supply the Setegusa steel mill in Sete Lagoas, Minas Gerais.

4.4. Factors Contributing to the Abandonment of Farmlands

During the field campaign, no single predominant factor was identified as responsible for the abandonment of eucalyptus plantations in the municipality. A plausible explanation is the relatively low and declining charcoal prices between August 2018 and September 2020 (Figure 9). During this period, the average charcoal price was USD 79.00 per ton, considerably lower than in the subsequent period from September 2022 to May 2023, when prices increased sharply to an average of USD 166.00 per ton. This price was likely influenced by the global energy crisis caused by rising energy demand during the COVID-19 pandemic (2020–2023) as well as by the Russia-Ukraine conflict, which began in February 2022.

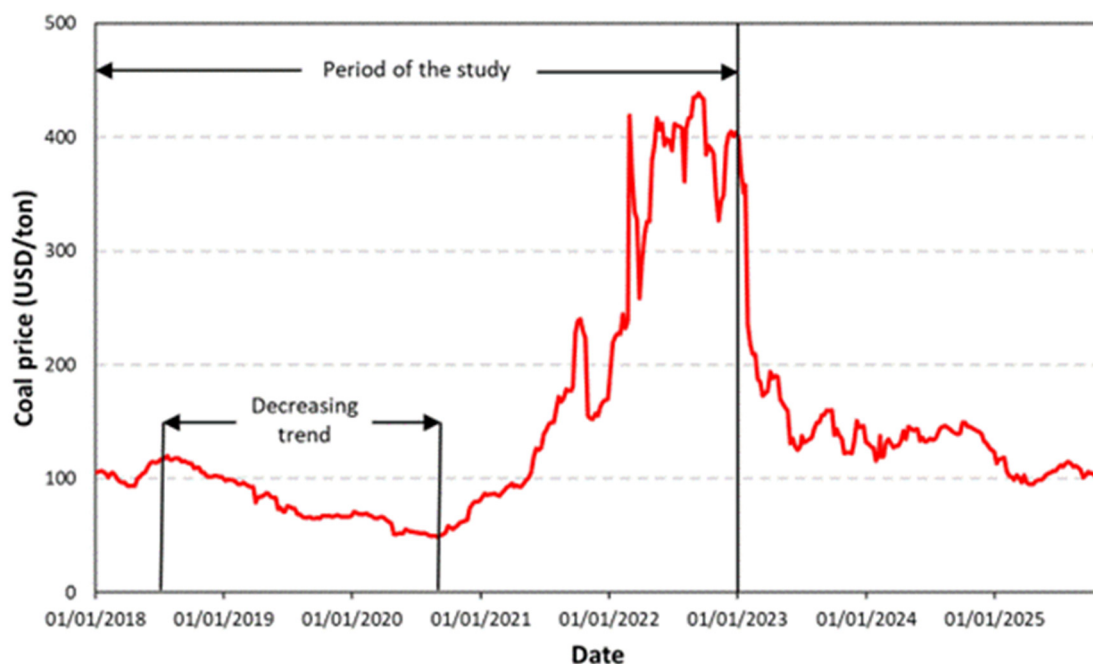


Figure 9. Charcoal prices in USD per ton over roughly last decade (2016–2025). Source: Trading Economics [75].

Information obtained from local farmers indicates that the main factors driving pasture abandonment include the high costs of limestone and chemical fertilizers required to maintain adequate pasture carrying capacity, combined with prolonged dry periods that sharply reduce forage growth and force producers to purchase silage during the dry season. Table 5 shows that beef production in Brazil has become increasingly expensive over the 2018–2022 period as a result of rising input costs, especially fertilizer price spikes, which nearly tripled between 2018 and 2022.

Table 5. Average beef price and input costs (USD per ton) in Brazil during the 2018–2022 period.

Year	Beef (USD/Ton)	Fertilizer (USD/Ton)	Corn Silage (USD/Ton)
2018	2639.33	361.00	90.00
2019	2752.00	507.61	222.40
2020	2933.33	314.20	134.20
2021	3578.00	758.30	224.65
2022	4066.00	988.37	217.00

Source: CEPEA [76].

4.5. Implications and Limitations

Economic factors associated with the abandoned farmlands identified in this study, such as the sharp increase in fertilizer prices and the reduced profitability of eucalyptus-based charcoal production, highlight the need for public policies that mitigate input cost volatility and strengthen the economic resilience of small- and medium-sized farmers. Abandoned farmlands often undergo natural regeneration, contributing to carbon sequestration, biodiversity recovery, and the enhancement of ecosystem services. The maps generated in this study can support policymakers in integrating abandoned areas into carbon sequestration accounting and climate mitigation strategies, as well as identifying regions suitable for passive restoration and the establishment of conservation corridors. Such applications align land management decisions with national and international commitments related to climate change and biodiversity conservation in the Cerrado.

We also emphasize the need for species-specific assessments of natural regeneration, particularly focusing on the successional dynamics of Cerrado woody and herbaceous species in areas previously subjected to intensive silviculture or grazing. Given that soil degradation is a major driver of farmland abandonment in the region, we recommend that future studies incorporate soil property monitoring, including nutrient status, compaction, organic carbon recovery, and erosion susceptibility.

Despite these contributions, several important limitations should be acknowledged. First, the analysis relies on only two Sentinel-2 acquisition dates (2018 and 2022) to infer farmland abandonment. The lack of intermediate observations means that areas reclassified as grassland or shrubland in 2022 were assumed to have remained uncultivated for the entire five-year period. This assumption may lead to an overestimation of permanent abandonment, as it does not distinguish long-term abandonment from temporary fallow or short-term land use transitions. Future studies would benefit from incorporating denser temporal series, ideally with annual or seasonal intervals.

Second, although the FCNN-based LULC classification was rigorously validated, the validation of the abandonment map relied essentially on visual inspection of high-resolution Google Earth images for polygons larger than 10 hectares. Because abandonment is inherently linked to management practices, spectral signatures alone may be ambiguous. Therefore, field-based validation, although time-consuming and costly, is recommended to complement remote sensing interpretation and improve the reliability of abandonment assessments.

Third, although field data collected during two field campaigns in 2023 were used for the calibration and validation of the FCNN-based LULC classification, the validation of the abandoned farmland map relied exclusively on high-resolution images available on the Google Earth platform. This dependence on remote interpretation may introduce uncertainties, especially in areas where management practices cannot be inferred solely from spectral or visual inspection.

Finally, the detailed spatial characterization of abandoned farmlands produced in this study offers valuable support for regional planning and restoration initiatives. These maps can assist government agencies, environmental planners, and landowners in prioritizing areas for rehabilitation, including degraded eucalyptus plantations and underperforming pasturelands. This is especially relevant for Brazil's National Program for Conversion of Degraded Pastures (PNCPD), a national initiative aimed at restoring 40 million hectares of degraded pastures (Decree No. 11.687/2023).

The methodological framework presented here also provides a replicable approach for improving municipal- and state-level land use inventories, identifying abandonment hotspots associated with economic pressures, and supporting ecological assessments related to natural regeneration, carbon accumulation, soil degradation recovery, and habitat connectivity in landscapes undergoing agricultural contraction.

5. Conclusions

This study demonstrated the applicability and robustness of the FCNN classifier for mapping abandoned farmlands in the Brazilian Cerrado using Sentinel-2 multispectral images. By integrating spectral indices, spectral mixture components, and principal components into a deep learning architecture, the approach achieved strong classification performance (overall accuracy = 76.3%). The results indicated that farmland abandonment between 2018 and 2022, totaling 13,147 hectares, or 4.7% of the agricultural land area in 2018, was predominantly associated with eucalyptus plantations, whereas no evidence of abandonment was detected for annual croplands. These findings highlight the suitability of deep learning methods for capturing subtle land use transitions in complex tropical savanna environments.

Discriminating pasture abandonment remains challenging because of the spectral similarity among degraded pastures, active pastures, and natural grasslands and shrublands. Improving monitoring accuracy will require higher spatiotemporal resolution datasets. In addition to its scientific contributions, the cartographic products generated in this study provide a valuable tool for regional land use planning and environmental management in the Cerrado, offering precise spatial information of abandoned lands to support decision-making processes related to agricultural restoration. Investigating the persistence of abandonment over longer timeframes is essential for understanding its implications for carbon sequestration and biodiversity conservation in the Cerrado biome.

Author Contributions: Conceptualization, E.E.S.; methodology, E.E.S. and I.A.L.M.; software, I.A.L.M.; validation, E.E.S. and I.A.L.M.; formal analysis, E.E.S.; investigation, I.A.L.M. and E.E.S.; resources, E.E.S.; data curation, E.E.S.; writing—original draft preparation, I.A.L.M.; writing—review and editing, E.E.S., É.L.B. and G.B.; visualization, E.E.S., É.L.B. and G.B.; supervision, E.E.S.; project administration, E.E.S.; funding acquisition, E.E.S. All authors have read and agreed to the published version of the manuscript.

Funding: This research was funded by the Foundation for Research Support of the Federal District (FAPDF), under Processes No. 00193.00002276/2022-90 and 00193.00002586/2022-12. The National Council for Scientific and Technological Development (CNPq) provided research productivity fellowship (PQ) for E.E.S. (Process No. 307850/2023-4) and É.L.B. (Process No. 302963/2025-1).

Data Availability Statement: The data and maps will be available upon request for the corresponding author.

Acknowledgments: We thank the anonymous reviewers for the important suggestions. ChatGPT-5 Plus (OpenAI) was used exclusively to assist with English language editing. No AI tool was used for data analysis, interpretation, or the generation of scientific content.

Conflicts of Interest: Authors (Edson Eyji Sano, Édson Luis Bolfe and Gustavo Bayma) are employed by Brazilian Agricultural Research Corporation. The remaining authors declare that the research was conducted in the absence of any commercial or financial relationships that could be construed as a potential conflict of interest.

Abbreviations

The following abbreviations are used in this manuscript:

BRDF	Bidirectional Reflectance Distribution Function
BSI	Bare Soil Index
CNN	Convolutional Neural Network
ESA	European Space Agency
EVI	Enhanced Vegetation Index
FCNN	Fully Connected Neural Network
GPD	Gross Domestic Product
GPS	Global Positioning System
INPE	National Institute for Space Research
KNN	K-Nearest Neighbors
LSMM	Linear Spectral Mixture Model
LULC	Land Use and Land Cover
MSI	Multispectral Imager
NDVI	Normalized Difference Vegetation Index
NDWI	Normalized Difference Water Index
NIR	Near-infrared
PCA	Principal Component Analysis
ReLU	Rectified Linear Unit
RF	Random Forest
SNAP	Sentinel Application
SVM	Support Vector Machine
SWIR	Shortwave infrared
UTM	Universal Transverse of Mercator

References

1. Huang, Y.; Li, F.; Xie, H. A scientometrics review on farmland abandonment research. *Land* **2020**, *9*, 263. [CrossRef]
2. Prishchepov, A.V.; Schierhorn, F.; Low, F. Unraveling the diversity of trajectories and drivers of global agricultural land abandonment. *Land* **2021**, *10*, 97. [CrossRef]
3. Zheng, Q.; Ha, T.; Prishchepov, V.; Zeng, Y.; Yin, H.; Koh, L.P. The neglected role of abandoned cropland in supporting both food security and climate change mitigation. *Nat. Commun.* **2023**, *14*, 6083. [CrossRef] [PubMed]
4. Yu, H.; Zhao, Z.; Yang, Q. Drivers and mechanisms of cropland abandonment in typical mountainous areas of Southwestern China. *Front. Sustain. Food Syst.* **2025**, *9*, 1614067. [CrossRef]
5. Haddaway, N.R.; Styles, D.; Pullin, A.S. Environmental impacts of farm land abandonment in high altitude/mountain regions: A systematic map of the evidence. *Environ. Evid.* **2013**, *2*, 18. [CrossRef]
6. Keenleyside, C.; Tucker, G. *Farmland Abandonment in the EU: An Assessment of Trends and Prospects*; Report prepared for WWF; Institute for European Environmental Policy: London, UK, 2010. Available online: https://scholar.google.com/scholar_lookup?title=Farmland+Abandonment+in+the+EU:+An+Assessment+of+Trends+and+Prospects&author=Keenleyside,+C.&author=Tucker,+G.&publication_year=2010 (accessed on 30 November 2025).
7. Ojha, R.B.; Atreya, K.; Kristiansen, P.; Devkota, D.; Wilson, B. A systematic review and gap analysis of drivers, impacts, and restoration options for abandoned croplands in Nepal. *Land Use Policy* **2022**, *120*, 106237. [CrossRef]

8. Liu, T.; Yu, L.; Liu, X.; Peng, D.; Chen, X.; Du, Z.; Tu, Y.; Wu, H.; Zhao, Q. A global review of monitoring cropland abandonment using remote sensing: Temporal-spatial patterns, causes, ecological effects, and future prospects. *J. Remote Sens.* **2025**, *5*, 0584. [CrossRef]
9. Wu, X.; Zhao, N.; Wang, Y.; Ye, Y.; Wang, W.; Yue, T.; Zhang, L.; Liu, Y. The potential role of abandoned cropland for food security in China. *Resour. Conserv. Recycl.* **2025**, *212*, 108004. [CrossRef]
10. Zhou, H.; Wang, J.; Sun, M.; Wang, J.; Yang, K. Evolution of farmland abandonment research from 1993 to 2023 using CiteSpace-based scientometric analysis. *J. Geovis. Spat. Anal.* **2004**, *8*, 20. [CrossRef]
11. Goga, T.; Feranec, J.; Bucha, T.; Rusnák, M.; Sačkov, I.; Barka, I.; Kopecká, M.; Papčo, J.; Ot'ahel', J.; Szatmári, D.; et al. A review of the application of remote sensing data for abandoned agricultural land identification with focus on central and eastern Europe. *Remote Sens.* **2019**, *11*, 2759. [CrossRef]
12. Yin, H.; Brandão, A., Jr.; Buchner, J.; Helmers, D.; Iuliano, B.G.; Kimambo, N.E.; Lewińska, K.E.; Razenkova, E.; Rizayeva, A.; Rogova, N.; et al. Monitoring cropland abandonment with Landsat time series. *Remote Sens. Environ.* **2020**, *24*, 111873. [CrossRef]
13. Xie, Y.; Spawn-Lee, S.A.; Radeloff, V.C.; Yin, H.; Robertson, G.P.; Lark, T.J. Cropland abandonment between 1986 and 2018 across the United States: Spatiotemporal patterns and current land uses. *Environ. Res. Lett.* **2024**, *19*, 044009. [CrossRef]
14. Li, S.; Li, X.; Sun, L.; Cao, G.; Fischer, G.; Tramberend, S. An estimation of the extent of cropland abandonment in mountainous regions of China. *Land Degrad. Dev.* **2018**, *29*, 1327–1342. [CrossRef]
15. Krysiak, S.; Papinska, E.; Majchrowska, A.; Adamiak, M.; Koziarkiewicz, M. Detecting land abandonment in Łódź Voivodeship using convolutional neural networks. *Land* **2020**, *9*, 82. [CrossRef]
16. Rada, N. Assessing Brazil's Cerrado agricultural miracle. *Food Policy* **2013**, *38*, 146–155. [CrossRef]
17. Zalles, V.; Hansen, M.C.; Potapov, P.V.; Stehman, S.V.; Tyukavina, A.; Pickens, A.; Song, X.-P.; Adusei, B.; Okpa, C.; Aguilar, R.; et al. Near doubling of Brazil's intensive row crop area since 2000. *Proc. Natl. Acad. Sci. USA* **2019**, *116*, 428–435. [CrossRef]
18. Instituto Brasileiro de Geografia e Estatística (IBGE). PAM—Produção Agrícola Municipal; IBGE: Rio de Janeiro, Brazil, 2025. Available online: <https://www.ibge.gov.br/estatisticas/economicas/agricultura-e-pecuaria/9117-producao-agricola-municipal-culturas-temporarias-e-permanentes.html> (accessed on 30 November 2025).
19. Myers, N.; Mittermeier, R.A.; Mittermeier, C.G.; Fonseca, G.A.B.; Kent, J. Biodiversity hotspots for conservation priorities. *Nature* **2000**, *403*, 853–858. [CrossRef]
20. Sano, E.E.; Rosa, R.; Brito, J.L.S.; Ferreira, L.G. Land cover mapping of the tropical savanna region in Brazil. *Environ. Monit. Assess.* **2010**, *166*, 113–124. [CrossRef]
21. Rausch, L.L.; Gibbs, H.K.; Schelly, I.; Brandão, A., Jr.; Morton, D.C.; Carneiro Filho, A.; Strassburg, B.; Walker, N.; Noojipady, P.; Barreto, P.; et al. Soy expansion in Brazil's Cerrado. *Conserv. Lett.* **2019**, *12*, e12671. [CrossRef]
22. Rodrigues, A.A.; Macedo, M.N.; Silvério, D.V.; Maracahipes, L.; Coe, M.T.; Brando, P.M.; Shimbo, J.Z.; Rajão, R.; Soares-Filho, B.; Bustamante, M.M.C. Cerrado deforestation threatens regional climate and water availability for agriculture and ecosystems. *Glob. Change Biol.* **2022**, *28*, 6807–6822. [CrossRef]
23. Althoff, D.; Rodrigues, L.N.; Silva, D.D. Assessment of water availability vulnerability in the Cerrado. *Appl. Water Sci.* **2021**, *11*, 176. [CrossRef]
24. Santos, J.F.S.; Naval, L.P. Soy water footprint and socioeconomic development: An analysis in the new agricultural expansion areas of the Brazilian cerrado (*Brazilian savanna*). *Environ. Dev.* **2022**, *42*, 100670. [CrossRef]
25. Sano, E.E.; Bettiol, G.M.; Bolfe, E.L.; Parreiras, T.C.; Cho, D.F. Mudanças de uso nas áreas agrícolas do Cerrado no período 2016–2020. In Proceedings of the XX Simpósio Brasileiro de Sensoriamento Remoto (SBSR), Florianópolis, Brazil, 2–5 April 2023; INPE: Florianópolis, SC, Brazil, 2023; pp. 1049–1052.
26. Costa, L.C.; Cunha, A.P.M.A.; Anderson, L.O.; Cunningham, C. New approach for drought assessment: A case study in the northern region of Minas Gerais. *Int. J. Disaster Risk Reduct.* **2021**, *53*, 102019. [CrossRef]
27. Carvalho Júnior, F.V.; Alves, M.C.; Carvalho, L.G. Analysis of rainfall variations and coffee production areas with climate change in Minas Gerais via future scenarios. *Theor. Appl. Climatol.* **2024**, *155*, 5887–5908. [CrossRef]
28. Leite, M.E.; Almeida, J.W.L.; Silva, R.F. Análise espaço-temporal do eucalipto no Norte de Minas Gerais nos anos de 1986, 1996 e 2010. *GeoTextos* **2012**, *8*, 59–74. [CrossRef]
29. Alencar, A.; Shimbo, J.Z.; Lenti, F.; Marques, C.B.; Zimbres, B.; Rosa, M.; Arruda, V.; Castro, I.; Ribeiro, J.P.F.M.; Varella, V.; et al. Mapping three decades of changes in the Brazilian savanna native vegetation using Landsat data processed in the Google Earth Engine platform. *Remote Sens.* **2020**, *12*, 924. [CrossRef]
30. Matosak, B.M.; Fonseca, L.M.G.; Taquary, E.C.; Maretto, R.V.; Bendini, H.N.; Adami, M. Mapping deforestation in Cerrado based on hybrid deep learning architecture and medium spatial resolution satellite time series. *Remote Sens.* **2022**, *14*, 209. [CrossRef]
31. Sheykhmousa, M.; Mahdianpari, M.; Ghanbari, H.; Mohammadimanesh, F.; Ghamisi, P.; Homayouni, S. Support Vector Machine versus Random Forest for remote sensing image classification: A meta-analysis and systematic review. *IEEE J. Sel. Top. Appl. Earth Obs. Remote Sens.* **2020**, *13*, 6308–6325. [CrossRef]

32. Xie, G.; Niculescu, S. Mapping and monitoring of land cover/land use (LCLU) changes in the Crozon Peninsula (Brittany, France) from 2007 to 2018 by machine learning algorithms (Support Vector Machine, Random Forest, and Convolutional Neural Network) and by post-classification comparison (PCC). *Remote Sens.* **2021**, *13*, 3899. [\[CrossRef\]](#)
33. Santos, L.F.; Ruchkys, U.A. A geospatial insight into farmland abandonment in Matopiba: The emerging frontier of Brazilian agriculture. *Reg. Environ. Change* **2025**, *25*, 66. [\[CrossRef\]](#)
34. Lei, X.; Fan, Y.; Li, K.C.; Castiglione, A.; Hu, Q. High-precision linearized interpretation for fully connected neural network. *Appl. Soft Comput.* **2021**, *109*, 107572. [\[CrossRef\]](#)
35. Zhang, C.; Yi, M.; Ye, F.; Xu, Q.; Li, X.; Gan, Q. Application and evaluation of deep neural networks for airborne hyperspectral remote sensing mineral mapping: A case study of the Baiyanghe uranium deposit in Northwestern Xinjiang, China. *Remote Sens.* **2022**, *14*, 5122. [\[CrossRef\]](#)
36. Judith, J.; Tamilselvi, R.; Beham, M.P.; Lakshmi, S.S.P.; Panthakkan, A.; Mansoon, S.A.; Ahmad, H.A. Remote sensing based crop health classification using NDVI and fully connected neural networks. *Int. Arch. Photogramm. Remote Sens. Spat. Inf. Sci.* **2025**, *XLVIII-G-2025*, 739–747. [\[CrossRef\]](#)
37. Yang, L.; Liu, M.; Liu, N.; Guo, J.; Lin, L.; Zhang, Y.; Du, X.; Xu, Y.; Zhu, C.; Wang, Y. Recovering bathymetry from satellite altimetry-derived gravity by fully connected deep neural network. *IEEE Geosci. Remote Sens. Lett.* **2023**, *20*, 1502805. [\[CrossRef\]](#)
38. Chacón-Maldonado, A.M.; Asencio-Cortés, G.; Troncoso, A. A multimodal hybrid deep learning approach for pest forecasting using time series and satellite images. *Inf. Fusion* **2025**, *124*, 103350. [\[CrossRef\]](#)
39. Wei, Z.; Gu, X.; Sun, Q.; Hu, X.; Gao, Y. Analysis of spatial and temporal pattern of changes in abandoned farmland based on long-time series of remote sensing data. *Remote Sens.* **2021**, *13*, 2549. [\[CrossRef\]](#)
40. Fayet, C.M.J.; Reilly, K.H.; Van Ham, C.; Verburg, P.H. What is the future of abandoned agricultural lands? A systematic review of alternative trajectories in Europe. *Land Use Policy* **2022**, *112*, 105833. [\[CrossRef\]](#)
41. Subedi, Y.R.; Kristiansen, P.; Cacho, O. Drivers and consequences of agricultural land abandonment and its reutilization pathways: A systematic review. *Environ. Dev.* **2022**, *42*, 100681. [\[CrossRef\]](#)
42. Alvares, C.A.; Stape, J.L.; Sentelhas, P.C.; Moraes, J.L.G.; Sparovek, G. Köppen's climate classification map for Brazil. *Meteorol. Z.* **2014**, *22*, 711–728. [\[CrossRef\]](#)
43. Rouse, J.W.; Haas, R.H.; Scheel, J.A.; Deering, D.W. Monitoring vegetation systems in the Great Plains with ERTS. In Proceedings of the 3rd Earth Resource Technology Satellite (ERTS) Symposium, Washington, DC, USA, 10–14 December 1973; NASA SP-351. NASA: Washington, DC, USA, 1974; Volume 1, pp. 48–62.
44. Tucker, C.J. Red and photographic infrared linear combinations for monitoring vegetation. *Remote Sens. Environ.* **1979**, *8*, 127–150. [\[CrossRef\]](#)
45. Huete, A.; Kidan, K.; Miura, T.; Rodriguez, E.P.; Gao, X.; Ferreira, L.G. Overview of the radiometric and biophysical performance of the MODIS vegetation indices. *Remote Sens. Environ.* **2002**, *83*, 195–213. [\[CrossRef\]](#)
46. Sangpradid, S. Change vector analysis using integrated vegetation indices for land cover change detection. *Int. J. Geoinform.* **2018**, *14*, 71–77.
47. Polykretis, C.; Grillakis, M.G.; Alexakis, D.D. Exploring the impact of various spectral indices on land cover change detection using change vector analysis: A case study of Crete Island, Greece. *Remote Sens.* **2020**, *12*, 319. [\[CrossRef\]](#)
48. Gao, B.C. NDWI—A Normalized Difference Water Index for remote sensing of vegetation liquid water from space. *Remote Sens. Environ.* **1996**, *58*, 257–266. [\[CrossRef\]](#)
49. Drusch, M.; Del Bello, U.; Carlier, S.; Colin, O.; Fernandez, V.; Gascon, F.; Hoersch, B.; Isola, C.; Laberinti, P.; Martimort, P.; et al. Sentinel-2: ESA's optical high-resolution mission for GMES operational services. *Remote Sens. Environ.* **2012**, *120*, 25–36. [\[CrossRef\]](#)
50. European Space Agency (ESA). *Copernicus Sentinel-2 Collection 1 MSI Level-2A (L2A)*; ESA: Paris, France, 2021. Available online: <https://sentinels.copernicus.eu/sentinel-data-access/sentinel-products/sentinel-2-data-products/collection-1-level-2a> (accessed on 15 September 2025).
51. Instituto Brasileiro de Geografia e Estatística (IBGE). *Downloads Geociências*; IBGE: Rio de Janeiro, Brazil, 2024. Available online: https://geoftp.ibge.gov.br/organizacao_do_territorio/malhas_territoriais/malhas_municipais/municipio_2024/Brasil/ (accessed on 12 July 2025).
52. Shimabukuro, Y.E.; Smith, J.A. The least-square mixing models to generate fraction images derived from remote sensing multispectral data. *IEEE Trans. Geosci. Remote Sens.* **1991**, *29*, 16–20. [\[CrossRef\]](#)
53. Shimabukuro, Y.E.; Arai, E.; Silva, G.M.; Hoffmann, T.B.; Duarte, V.; Dutra, A.C.; Adami, M. Monitoring annual Landsat-based deforestation using LMSS and MODIS-burned area product in Rondônia, Brazilian Amazon. *Discov. Conserv.* **2025**, *2*, 21. [\[CrossRef\]](#)
54. Murariu, G.; Dinca, L.; Munteanu, D. Trends and applications of principal component analysis in forestry research: A literature review and bibliometric review. *Remote Sens.* **2025**, *16*, 1155. [\[CrossRef\]](#)

55. Maggiori, E.; Tarabalka, Y.; Charpiat, G.; Alliez, P. Fully convolutional neural networks for remote sensing image classification. In Proceedings of the 2016 IEEE International Geoscience and Remote Sensing Symposium (IGARSS), Beijing, China, 10–15 July 2016; IEEE: Beijing, China, 2016; pp. 5071–5074.
56. Takada, T.; Miyamoto, A.; Hasegawa, S.F. Derivation of a yearly transition probability matrix for land-use dynamics and its applications. *Landsc. Ecol.* **2010**, *25*, 561–572. [\[CrossRef\]](#)
57. Puyravaud, J.P. Standardizing the calculation of the annual rate of deforestation. *For. Ecol. Manag.* **2003**, *177*, 593–596. [\[CrossRef\]](#)
58. Lemessa, D. A robust method of computing the annual rate of land use/land covers change in landscapes. *East Afr. J. Sci.* **2020**, *14*, 163–168.
59. Xinchang, Z.; Qiong, P.; Yuan, Z. Research on spatial calculating analysis model of landuse change. *J. Geogr. Sci.* **2004**, *14*, 359–365. [\[CrossRef\]](#)
60. Foody, G.M. Status of land cover classification accuracy assessment. *Remote Sens. Environ.* **2002**, *80*, 185–201. [\[CrossRef\]](#)
61. Comber, A.; Fisher, P.; Brunsdon, C.; Khmag, A. Spatial analysis of remote sensing image classification accuracy. *Remote Sens. Environ.* **2012**, *127*, 237–246. [\[CrossRef\]](#)
62. Ribeiro, J.F.; Walter, B.M.T. Fitofisionomias do bioma Cerrado. In *Cerrado: Ecologia e Flora*; Sano, S.M., Almeida, S.P., Ribeiro, J.F., Eds.; Embrapa-CPAC: Planaltina, Brazil, 2008; Volume 1, pp. 151–212.
63. MapBiomass. Codes of the Legend Classes and Color Palette Used in MapBiomass Collection 7. 2025. Available online: https://brasil.mapbiomas.org/wp-content/uploads/sites/4/2023/08/EN_Codigos_da_Legenda_Colecao_7.pdf (accessed on 15 October 2025).
64. Souza, C.M.; Shimbo, J.Z.; Rosa, M.R.; Parente, L.L.; Alencar, A.; Rudorff, B.F.; Hasenack, H.; Matsumoto, M.; Ferreira, L.G.; E Souza-Filho, P.W.; et al. Reconstructing three decades of land use and land cover changes in Brazilian biomes with Landsat archive and Earth Engine. *Remote Sens.* **2020**, *12*, 2735. [\[CrossRef\]](#)
65. Jacon, A.D.; Galvão, L.S.; Dalagnol, R.; Santos, J.R. Aboveground biomass estimates over Brazilian savannas using hyperspectral metrics and machine learning models: Experiences with Hyperion/EO-1. *GISci. Remote Sens.* **2021**, *58*, 112–1129. [\[CrossRef\]](#)
66. Araújo, J.A.; Galvão, L.S.; Dalagnol, R. Sensitivity of hyperspectral vegetation indices to rainfall seasonality in the Brazilian savannahs: An analysis using PRISMA data. *Remote Sens. Lett.* **2023**, *14*, 277–287. [\[CrossRef\]](#)
67. Sano, E.E.; Magalhães, I.A.L.; Rodrigues, L.N.; Bolfe, E.L. Spatio-temporal dynamics of center pivot irrigation systems in the Brazilian tropical savanna (1985–2020). *Water* **2024**, *16*, 1897. [\[CrossRef\]](#)
68. Arruda, V.L.S.; Alencar, A.A.C.; Carvalho Júnior, O.A.; Ribeiro, F.F.; Arruda, F.V.; Conciani, D.E.; Silva, W.V.; Shimbo, J.Z. Assessing four decades of fire behavior dynamics in the Cerrado biome (1985 to 2022). *Fire Ecol.* **2024**, *20*, 64. [\[CrossRef\]](#)
69. Landis, J.R.; Koch, G.G. The measurement of observer agreement for categorical data. *Biometrics* **1977**, *33*, 159–174. [\[CrossRef\]](#)
70. Altman, D. *Practical Statistics for Medical Research*; CRC Press: Boca Raton, FL, USA, 1999.
71. Basheer, S.; Wang, X.; Farooque, A.A.; Nawaz, R.A.; Liu, K.; Adekanmbi, T.; Liu, S. Comparison of land use and land cover classifiers using different satellite imagery and machine learning techniques. *Remote Sens.* **2022**, *14*, 4978. [\[CrossRef\]](#)
72. Zhao, Z.; Islam, F.; Waseem, L.A.; Tariq, A.; Nawaz, M.; Islam, I.U.; Bibi, T.; Rehman, N.U.; Ahmad, W.; Aslam, R.W.; et al. Comparison of three machine learning algorithms using Google Earth Engine for land use and land cover classification. *Rangel. Ecol. Manag.* **2024**, *92*, 129–137. [\[CrossRef\]](#)
73. Silva, N.F.; Barros, N.F.; Neves, J.C.L.; Schulthais, F.; Novais, R.F.; Mattiello, E.M. Yield and nutrient demand and efficiency of eucalyptus under coppicing regime. *Forests* **2020**, *11*, 852. [\[CrossRef\]](#)
74. Ricardo, H.C.; Charles, T.S.; Lopes, T.R.; Mendonça, F.C.; Machado, R.E.; Duarte, S.N. Agricultural expansion and possible effects on hydrological services: A case study of the MATOPIBA region, Brazil. *Ecolhydrol. Hydrobiol.* **2025**, *25*, 100693. [\[CrossRef\]](#)
75. Trading Economics. *Coal (USD/Tonne)*; Trading Economics: New York, NY, USA, 2025. Available online: <https://pt.tradingeconomics.com/commodity/coal> (accessed on 30 October 2025).
76. Centro de Estudos Avançados em Economia Aplicada (Cepea). *Indicadores de Preços Agropecuários*; Centro de Estudos Avançados em Economia Aplicada: Piracicaba, Brazil, 2025. Available online: <https://www.cepea.esalq.usp.br/> (accessed on 10 November 2025).

Disclaimer/Publisher’s Note: The statements, opinions and data contained in all publications are solely those of the individual author(s) and contributor(s) and not of MDPI and/or the editor(s). MDPI and/or the editor(s) disclaim responsibility for any injury to people or property resulting from any ideas, methods, instructions or products referred to in the content.